Strongly superadiabatic and stratified limits of compressible convection

John Panickacheril John [1] and Jörg Schumacher [1,2,*]

[1]*Institut für Thermo- und Fluiddynamik, Technische Universität Ilmenau, D-98684 Ilmenau, Germany*
[2]*Tandon School of Engineering, New York University, New York, New York 11201, USA*

Fully compressible turbulent convection beyond the Oberbeck-Boussinesq limit and anelastic regime is studied in three-dimensional numerical simulations. Superadiabaticity ϵ and dissipation number D, which measures the strength of stratification of adiabatic equilibria, cause two limits of compressible convection—nearly top-down-symmetric, strongly superadiabatic convection and highly top-down-asymmetric, strongly stratified convection. The highest turbulent Mach numbers M_t follow for a symmetric blend of these two limits, which we term the fully compressible case. Particularly, the strongly stratified convection case leads to a fluctuation-reduced top layer in the convection zone, a strongly reduced global heat transfer, and differing boundary layer dynamics between top and bottom. We detect this asymmetry for growing dissipation number D also in the phase plane, which is spanned by the turbulent Mach number M_t and the dilatation parameter δ, which relates the dilatational velocity fluctuations to the solenoidal ones. A detailed analysis of the different transport currents in the fully compressible energy budget relates the low-D convection cases to the standard definition of the dimensionless Nusselt number in the Oberbeck-Boussinesq limit.

I. INTRODUCTION

Buoyancy-driven turbulence significantly deviates, in most applications, from the thermal convection paradigm of a Rayleigh-Bénard layer heated from below and cooled from above [1]. The latter is characterized by small deviations from an (adiabatic) equilibrium state, incompressibility, and constant material properties, thus leading to a perfect statistical top-down symmetry, termed the Oberbeck-Boussinesq (OB) limit [2–5]. On the one hand, non-Oberbeck-Boussinesq (NOB) effects are caused by additional physical processes, such as phase changes in the atmosphere [6,7] which generate buoyancy reversals [8], or by strong dependencies of the material properties and density on temperature and pressure [9–13], e.g., in technical fluids for nuclear engineering [14]. On the other hand, they are also caused by compressibility [15], such as in giant gas planets [16,17] or the coupling of ocean mesoscale eddies to the surface wind stress fields of the lower atmosphere [18,19]. The corresponding numerical models typically involve the anelastic (AE) limit of the compressible flow case representing a small excess from the adiabatic equilibrium [20]. Other examples require a fully compressible treatment. Strong radiative cooling drives solar convection from the surface, causing downflows with characteristic velocity fluctuations reaching the speed of sound, $u' \sim c$ [21–24]. For supersonic convection (see, e.g., Refs. [25,26]) and for forced interstellar gas cloud turbulence with the velocity fluctuations up to $u' \lesssim 5c$, see Ref. [27].

In this work, we investigate fully compressible turbulent convection solely driven by buoyancy forces. The flow is characterized by the superadiabaticity, ϵ, and a measure of the stratification

---

*joerg.schumacher@tu-ilmenau.de

of density or temperature, the dissipation number D. Both parameters are bounded and form a triangular ϵ–D parameter plane. Buoyancy-driven compressible convection can thus proceed in two limits—the *strongly superadiabatic* (SAC) and the *strongly stratified convection* (SSC)—which lead to subsonic root-mean-square (rms) velocity amplitudes u'. Their mixture, which we will term *fully compressible convection* (FCC), is shown to result in the largest turbulent Mach numbers, $M_t = u'/c$. A first objective of the present work is consequently a systematic exploration of the ϵ–D parameter plane.

Variable material properties such as the temperature and pressure dependence of dynamic viscosity $\mu(T, p)$ and thermal conductivity $k(T, p)$ can also lead to non-Oberbeck-Boussinesq (NOB) behavior [4]. This is relevant in many astrophysical and geophysical systems, where we have gaseous systems with a complicated equation of state involving nontrivial dependencies of material properties on the thermodynamic state variables, T and p. They also differ from the usually assumed Sutherland law for ideal gases [28]. In reality, these variable fluid properties can interact with compressibility effects, which complicates a systematic analysis of the convection regimes. This is outside the scope of the present study. Here, we try to disentangle and isolate *genuine compressibility effects* from other possible routes to NOB convection [29] by keeping constant material parameters, μ_0 and k_0.

We also show that not every NOB flow will generate highly asymmetric mean vertical profiles of central turbulence quantities across the layer, even though the detaching thermal plumes are found to be asymmetric in all cases—thinner plumes detaching from the top in comparison to the ones from the bottom. We will use the Kullback-Leibler (KL) divergence [30] between the *local* boundary layer thickness distributions at top and bottom to access this asymmetry for all cases [31]. Finally, we analyze in detail the energy equation budget, such that we can compare the different currents with the diffusive and convective heat currents from the Rayleigh-Bénard convection case which is the OB limit with $\epsilon \to 0$ and, subsequently, $D \to 0$.

One motivation for the present study of the SSC is the interior of the Sun. In the upper layer, the turbulent Mach number is of $O(1)$ or partly even slightly larger at the surface to the coronal vacuum, possible due to a moderate superadiabaticity and extreme drops of temperature and density. The strong stratification, particularly in the upper convection zone, is in line with anomalously weak velocity fluctuations, as observed by helioseismology measurements [32] for solar radii $r \gtrsim 0.92 R_\odot$. By exploring the extreme limits of turbulent compressible convection, as done here in a much simpler setting, our results might suggest new pathways to better explain these observations, despite being orders of magnitude away from reality in terms of Rayleigh and Prandtl numbers. We will come back to this point in the final discussion of the work.

II. GOVERNING EQUATIONS

Our study is based on three-dimensional direct numerical simulations (DNS) of the fully compressible differential balance equations for mass, momentum, and internal energy densities, ρ, ρu_i, and ρe, by a compact finite-difference scheme [33–35] which is appropriate for subsonic flows [36]. The fully compressible Navier-Stokes equations along with the buoyancy term are given by

$$\frac{\partial \rho}{\partial t} + \frac{\partial (\rho u_i)}{\partial x_i} = 0, \tag{1a}$$

$$\frac{\partial (\rho u_i)}{\partial t} + \frac{\partial (\rho u_i u_j)}{\partial x_j} = -\frac{\partial p}{\partial x_i} + \frac{\partial \sigma_{ij}}{\partial x_j} - \rho g \delta_{i,3}, \tag{1b}$$

$$\frac{\partial (\rho e)}{\partial t} + \frac{\partial (\rho e u_j)}{\partial x_j} = -p \frac{\partial u_i}{\partial x_i} + \frac{\partial}{\partial x_i}\left(k \frac{\partial T}{\partial x_i}\right) + \sigma_{ij} S_{ij}, \tag{1c}$$

$$p = \rho R T \quad \text{where} \quad R = C_p - C_v, \tag{1d}$$

with $i, j = x, y, z$. These equations correspond to mass, momentum, and energy conservation laws along with the ideal gas equation of state. Here, ρ, u_i, p, ρe, and T are the density, components of the velocity field, pressure, internal energy density, and temperature, respectively. The specific internal energy is defined as $e = C_v T$. R is the gas constant. We used the Einstein summation convention. The viscous stress tensor σ_{ij} and strain rate tensor S_{ij} are defined as

$$\sigma_{ij} = \mu \left(\frac{\partial u_i}{\partial x_j} + \frac{\partial u_j}{\partial x_i} - \frac{2}{3} \delta_{ij} \frac{\partial u_k}{\partial x_k} \right) \quad \text{and} \quad S_{ij} = \frac{1}{2} \left(\frac{\partial u_i}{\partial x_j} + \frac{\partial u_j}{\partial x_i} \right), \tag{2}$$

respectively. The dynamic viscosity is assumed to be constant in these simulations, $\mu = \mu_0$. The thermal conductivity k is related to the viscosity through the Prandtl number, $k_0 = \mu_0 C_p / \text{Pr}$. In all our simulations, the Prandtl number is assumed to be $\text{Pr} = 0.7$. Here, g is the acceleration due to gravity, and C_p and C_v correspond to specific heat at constant pressure and volume, respectively. Their ratio, the adiabatic coefficient $\gamma = C_p / C_v = 1.4$, corresponds to a diatomic gas.

We have modified the code used in [37] for simulating channel flows. The space is discretized using horizontally uniform grids in the x and y directions, along with periodic boundary conditions. Along the wall normal direction, a nonuniform grid is used with clustering near the walls by using a hyperbolic tangent stretching function. The spatial derivatives are calculated using sixth-order compact finite differences for all points except near the walls. Fourth- and third-order compact schemes are used at the last two grid points near the wall, respectively. No-slip boundary conditions are used for the walls. The boundary condition for pressure is evaluated using the z-direction Navier-Stokes equations at the wall,

$$\frac{\partial p}{\partial z} = \frac{\partial \sigma_{iz}}{\partial x_i} - \rho g. \tag{3}$$

The variables are advanced in time using a low-storage third-order Runge-Kutta scheme. A Courant-Friedrichs-Lewy (CFL) number of 0.5 is used for all our direct numerical simulations. All the statistics are taken after the flow has reached the steady state.

III. COMPRESSIBLE CONVECTION REGIMES

The adiabatic equilibrium, for which the compressible convection layer is at rest, is given by $\bar{T}(z) = \bar{T}_{\text{bot}}(1 - Dz/H)$. The reference temperature is the adiabatic value at the bottom of the layer, $T_{\text{bot}} = \bar{T}_{\text{bot}}$. The first new dimensionless parameter D relates the dry adiabatic lapse rate g/C_p to a characteristic temperature drop across the convection layer of height H and thus measures the strength of stratification. It is termed the *dissipation number* [39] and is given by

$$D = \frac{gH}{C_p T_{\text{bot}}} = \frac{T_{\text{bot}} - \bar{T}_{\text{top}}}{T_{\text{bot}}}. \tag{4}$$

Bars denote plane-time averages of the adiabatic profiles. The actual value at the top differs with $T_{\text{top}} < \bar{T}_{\text{top}} (< T_{\text{bot}})$ for convection to occur. The second new dimensionless parameter in compressible convection is the *superadiabaticity* ϵ [39], which is defined as

$$\epsilon = \frac{\bar{T}_{\text{top}} - T_{\text{top}}}{T_{\text{bot}}}. \tag{5}$$

Note that $\epsilon \to 0$ corresponds to the anelastic limit, where the high-frequency acoustic motions are filtered out of the system. This is possible due to the scale separation between convective and acoustic motions at low ϵ. However, at a finite ϵ, acoustic motions can interact with the convective physics, which can lead to NOB behavior.

For incompressible Rayleigh Bénard convection, the limits $\epsilon \to 0$ and, subsequently, $D \to 0$ are taken [39]. Thus, NOB effects can be observed for finite magnitudes of both ϵ and D. From Eqs. (4) and (5), it is also clear that both dimensionless parameters satisfy $0 \leqslant \epsilon, D \leqslant 1$. Furthermore, we get $\epsilon + D = \Delta T / T_{\text{bot}} = (T_{\text{bot}} - T_{\text{top}}) / T_{\text{bot}}$. Thus, it follows immediately that $\epsilon \leqslant 1 - D$, which restricts
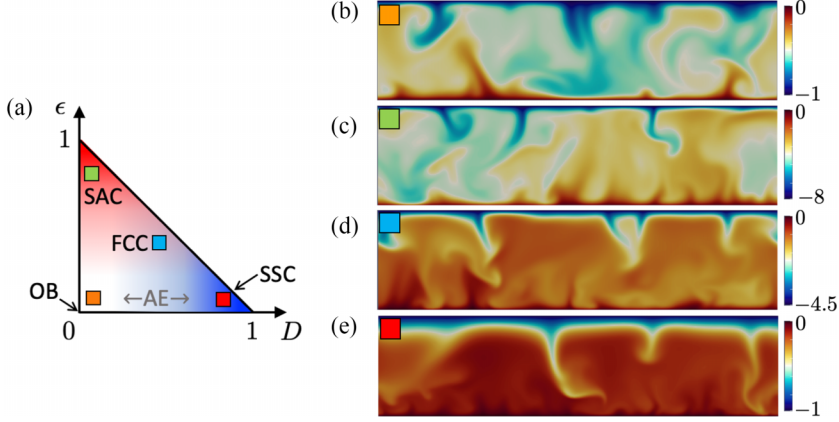
FIG. 1. Different regimes of compressible turbulent convection. (a) Parameter plane spanned by dissipation number D and superadiabaticity ϵ. The exact Oberbeck-Boussinesq limit (OB) at the origin and the anelastic (AE) regime are indicated together with the four different simulation cases. (b)–(e) Vertical slice cuts through (b) instantaneous temperature T_{sa} at $(\epsilon, D) = (0.1, 0.1)$ near the OB limit, (c) in highly superadiabatic convection (SAC) at $(0.8, 0.1)$, (d) in fully compressible convection at $(0.45, 0.5)$, and (e) in strongly stratified convection (SSC) at $(0.1, 0.8)$. The Rayleigh number is $\text{Ra} \simeq 10^6$ and the Prandtl number $\text{Pr} = 0.7$ in all cases.

the ϵ–D parameter plane to a triangle, as shown in Fig. 1(a). In this paper, we are interested in analyzing the limits of compressible convection in terms of both of the compressibility parameters. They are found in the corners of the parameter plane. When defining the free-fall velocity by $U_f = \sqrt{g\epsilon H}$ and the speed of sound by $c_s = \sqrt{\gamma R T_{\text{bot}}}$, a *free-fall Mach number* M_f can be defined [39]. The parameter M_f is given by

$$M_f = \frac{U_f}{c_s} = \sqrt{\frac{\epsilon D}{\gamma - 1}} \leqslant 1 \quad \text{for} \quad \epsilon, D \in [0, 1]. \tag{6}$$

Equation (6) shows that M_f is bounded from above by 1. For this bound, we use $\gamma = 7/5 = 1.4$ of an ideal gas and $\epsilon \leqslant 1 - D$. The maximum $M_f^* = \sqrt{5/8} \approx 0.79$ is obtained for a symmetric blend, $D = \epsilon = 1/2$. We can now identify different regimes of compressible thermal convection:

(1) *Oberbeck-Boussinesq-like convection* exists for $\epsilon \ll 1$ and $D \ll 1$ close to the exact OB Rayleigh-Bénard convection case at $(\epsilon, D) = (0, 0)$. This regime will be denoted, for simplicity, as OB or OB-like in this work. In this particular study, we take $\epsilon = D = 0.1$.

(2) *Strongly stratified convection* exists for $\epsilon \ll 1$ and $D \to 1$ and will be denoted as SSC. It is an extreme case of the AE limit that requires $\epsilon \ll 1$ only [39–41]. In this study, we take $\epsilon = 0.1$ and $D = 0.8$, the latter of which is still somewhat smaller than the maximum $D_{\text{max}} = 1 - \epsilon$ at fixed ϵ.

(3) *Fully compressible convection* exists for $\epsilon \approx D \approx 0.5$ and will be denoted as FCC. It is the range in which the free-fall Mach number is maximum. In this study, we take $\epsilon = 0.45$ and $D = 0.5$.

(4) *Strongly superadiabatic convection* exists for $D \ll 1$ and $\epsilon \to 1$ and will be abbreviated as SAC. In this study, we take $D = 0.1$ and $\epsilon = 0.8$, the latter of which is still somewhat smaller than the maximum $\epsilon_{\text{max}} = 1 - D$ at fixed D.

These four regimes of compressible convection are marked in the triangular $\epsilon - D$ phase plane in Fig. 1(a). The temperature ratio $T_{\text{bot}}/T_{\text{top}} = 1/[1 - (\epsilon + D)]$ varies from 1.25 to 20 in this study, as listed in Table I, where further details on all simulations are given. For all simulations, T_{bot} is kept constant. For the physics considered in this study, the absolute value of T_{bot} is not relevant.

It should be noted that $M_f \to 0$ when either ϵ or D go to zero. Our interest is in truly genuine compressible behavior limits with non-negligible Mach number. Thus, we have chosen finite values

TABLE I. List of eight compressible direct numerical simulations (DNS) along with the data from two incompressible RBC cases. The identifier, dissipation number D, superadiabaticity ϵ, ratio of temperature and density (adiabatic) at the bottom and top, maximum turbulent Mach number $M_t^{\max}$, Rayleigh number Ra, Prandtl number Pr, adiabatic coefficient γ, grid dimensions, Reynolds number Re, Nusselt number Nu, and number of horizontal grid planes inside the thermal boundary layers at the bottom and top are listed. All simulations have an aspect ratio of $\Gamma = L/H = 4$. The error bars for Re and Nu are obtained from the difference of the corresponding values of the two halves of the snapshot series. We add two Rayleigh-Bénard convection runs (subscript RBC) at the corresponding Rayleigh numbers which have been obtained by spectral element simulations [38] at $(D, \epsilon) = (0, 0)$ as references. Their grid resolution is given by the number of spectral elements times the number of collocation points on each spectral element in all three space directions.

No.	Identifier	D	ϵ	$T_{\text{bot}}/T_{\text{top}}$	$\bar{\rho}_{\text{bot}}/\bar{\rho}_{\text{top}}$	$M_t^{\max}$	Ra	Pr	γ	$N_x \times N_y \times N_z$	Re	Nu	No. λ_T^{bot}	No. λ_T^{top}
1_{RBC}	RBC	0	0			0	10^5	0.7	1.4	$256,000 \times 5^3$	94 ± 0.3	4.3 ± 0.02	66	66
1	OB	0.1	0.1	1.25	1.3	0.12	10^5	0.72	1.4	$256 \times 256 \times 128$	117 ± 0.8	4.0 ± 0.03	28	29
2	SAC	0.1	0.8	10	1.3	0.78	10^5	0.72	1.4	$256 \times 256 \times 128$	175 ± 2.1	5.1 ± 0.03	27	23
3	FCC	0.5	0.45	20	5.7	1.12	10^5	0.72	1.4	$256 \times 256 \times 128$	123 ± 0.3	4.0 ± 0.06	21	34
4	SSC	0.8	0.1	10	55.9	0.39	10^5	0.72	1.4	$256 \times 256 \times 128$	102 ± 1.5	2.8 ± 0.05	18	48
5_{RBC}	RBC	0	0			0	10^6	0.7	1.4	$256,000 \times 7^3$	296 ± 2.8	8.1 ± 0.06	58	58
5	OB	0.1	0.1	1.25	1.3	0.14	10^6	0.72	1.4	$512 \times 512 \times 256$	424 ± 3.9	7.9 ± 0.04	35	38
6	SAC	0.1	0.8	10	1.3	0.84	10^6	0.72	1.4	$512 \times 512 \times 256$	582 ± 2.6	9.9 ± 0.01	33	29
7	FCC	0.5	0.45	20	5.7	1.32	10^6	0.72	1.4	$512 \times 512 \times 256$	437 ± 3.9	8.0 ± 0.04	26	44
8	SSC	0.8	0.1	10	55.9	0.61	10^6	0.72	1.4	$512 \times 512 \times 256$	351 ± 3.1	4.3 ± 0.04	24	74

of $\epsilon = 0.1$ and $D = 0.1$ for the SSC and SAC cases, respectively. From Table I, it is seen that the obtained maximum turbulent Mach numbers are high enough such that approximations, including the pseudo-incompressible approximation [42,43], the low Mach number approximation of [44], or the anelastic [45] approximation, would not be valid. Indeed, finding out the ranges of validity of these approximations in the $\epsilon - D$ parameter plane and to study the transitions from these approximations to the fully compressible regime would be interesting and important. However, this is outside the scope of the present study; a brief discussion is included in the final discussion.

We furthermore note that the SAC and FCC regimes are relatively unexplored in the current literature. This is different from the SSC regime, which has been studied frequently in the past, e.g., in Refs. [39,46]. The present study extends the range of stratification in the SSC. In Table I, we provide the ratio of the background density stratification which is given by

$$\frac{\bar{\rho}_{\text{bot}}}{\bar{\rho}_{\text{top}}} = (1 - D)^{-1/(\gamma - 1)}, \tag{7}$$

for all simulations. For the SSC case, this ratio is about 56 compared to about 20 and 11 in Verhoeven *et al.* [39] and Cattaneo *et al.* [46], respectively. In Ref. [47], we showed a transition to the highly stratified convection when the dissipation number exceeds $D_{\text{crit}} \simeq 0.65$ (and $\bar{\rho}_{\text{bot}}/\bar{\rho}_{\text{top}} \geqslant 13.8$) for fixed $\epsilon \approx 0.1$ at Ra $= 10^6$. For the largest dissipation numbers, the pressure rather than the temperature fluctuations get synchronized with density fluctuations. Here, in our SSC case, $D = 0.8 > D_{\text{crit}}$, and thus our study will shed further light on the SSC limit case which includes a detailed analysis of the differences between the top and bottom boundary layers.

IV. SET OF DIRECT NUMERICAL SIMULATIONS

A total of eight DNS were conducted at two different Rayleigh numbers of Ra $\approx 10^5$ and 10^6 at Pr $= 0.72$ for each of the four regimes, with their operating points (ϵ, D); see, again, Table I. In addition, we add two corresponding Rayleigh-Bénard convection runs for reference, i.e., runs 1_{RBC}
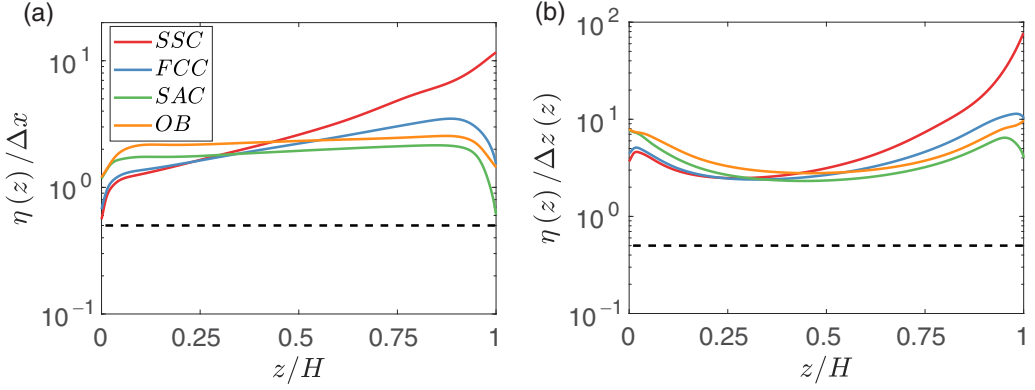
FIG. 2. Resolution of the DNS. Ratio of the height-dependent Kolmogorov length scale to (a) the uniform horizontal grid size and (b) the nonuniform wall-normal grid size. In both figures, the black dashed line corresponds to the resolution criterion from Ref. [34] at a ratio of 0.5. Data are for $Ra = 10^6$.

and 5_{RBC}. The dimensionless parameters Ra and Pr are given by

$$\text{Ra} = \frac{\epsilon \langle \rho \rangle_{V,t}^2 C_p g H^3}{\mu_0 k_0} \quad \text{and} \quad \text{Pr} = \frac{\mu_0 C_p}{k_0}. \tag{8}$$

The notation $\langle \rangle_{V,t}$ corresponds to a combined average with respect to full volume and time. For all simulations, we use an aspect ratio $\Gamma = L/H = 4$, where L is the horizontal length. Previous studies in isotropic compressible turbulence [34] have shown that a (uniform) grid resolution of $\eta/\Delta x \geqslant 0.5$ is sufficient to resolve the small-scale statistics correctly, such as moments of vorticity and dilatation up to fourth order. Here, η is the Kolmogorov length scale. In our case, the wall-normal grid spacing, $\Delta z(z)$, and the Kolmogorov length scale, $\eta(z)$, are functions of depth z. The latter is given by

$$\eta(z) = \left[\frac{\mu_0^3}{\rho_{\text{ref}}^3(z) \langle \epsilon_f(z) \rangle_{A,t}} \right]^{1/4}, \tag{9}$$

where $\rho_{\text{ref}}(z) = \langle \rho(z) \rangle_{A,t}$. The notation $\langle \cdot \rangle_{A,t}$ corresponds to a combined average over the horizontal directions and time, which is given for a field X as

$$\langle X(z) \rangle_{A,t} = \frac{\sum_{m=1}^{N_t} \sum_{i=1}^{N_x} \sum_{j=1}^{N_y} X(x_i, y_j, z, t_m)}{N_x N_y N_t}, \tag{10}$$

where N_x, N_y, and N_t are the grid point numbers with respect to the x and y directions, and number of snapshots, respectively.

The mean kinetic energy dissipation rate at height z is given by

$$\langle \epsilon_f(z) \rangle_{A,t} = \frac{\mu_0}{\langle \rho \rangle_{A,t}} \langle S_{ij} \sigma_{ij} \rangle_{A,t}. \tag{11}$$

The horizontal and vertical resolutions, $\eta/\Delta x$ and $\eta/\Delta z$, with respect to depth, are shown for $Ra \approx 10^6$ in Figs. 2(a) and 2(b), respectively. It is clear from both figures that for all cases, our simulations are very well resolved, i.e., the minimum ratio is above the threshold. The grid resolution in the wall-normal direction [Fig. 2(b)] is better than the one in the horizontal directions [Fig. 2(a)], due to much finer grid in the z direction. In Table I, we provide the number of grid points inside the top and bottom thermal boundary layers for all the simulations. The thermal boundary layer thicknesses

at the bottom and top are therefore defined as

$$\lambda_T^{\text{bot,top}} = |\langle T_{\text{sa}}(0,1) - T_{\text{sa}}(0.5)\rangle_{A,t}| \left|\frac{\partial \langle T_{\text{sa}}\rangle}{\partial z}\right|_{z/H=0,1}^{-1}. \tag{12}$$

Here, T_{sa} is the superadiabatic temperature, which is given by

$$T_{\text{sa}}(\mathbf{x}, t) = T(\mathbf{x}, t) - \overline{T}(z). \tag{13}$$

We can conclude that both boundary layers are very well resolved, which we also document in the last two columns of Table I; see, also, Ref. [38]. The present simulations are thus better resolved than those in [39].

V. SIMULATION RESULTS

A. Turbulent heat and momentum transfer—Nusselt and Reynolds number

The Nusselt and Reynolds numbers, Nu and Re, are the global responses of the system to the parameters Ra, Pr, D, and ϵ. They quantify the turbulent heat and momentum transfer. The Nusselt number is defined on the basis of the superadiabatic temperature field and is given by

$$\text{Nu} = -\frac{H}{\Delta \langle T_{\text{sa}}\rangle_{A,t}} \frac{d\langle T_{\text{sa}}\rangle_{A,t}}{dz}\bigg|_{z=0,H} = -\frac{H}{\epsilon T_B} \frac{d\langle T_{\text{sa}}\rangle_{A,t}}{dz}\bigg|_{z=0,H}. \tag{14}$$

The reported Nusselt number is the mean of those calculated at the top and bottom boundaries. The difference between both values was found to be negligible for all cases, with a range between 0.06% and 3%. This indicates that our simulations are well converged and statistically steady. The Reynolds number is defined as

$$\text{Re} = \frac{\rho_{\text{ref}} u' H}{\mu_0} \quad \text{with} \quad u' = \sqrt{\langle u_x^2\rangle_{V,t} + \langle u_y^2\rangle_{V,t} + \langle u_z^2\rangle_{V,t}}. \tag{15}$$

The Nusselt and Reynolds numbers for all cases are listed in Table I. For a given Ra, the SAC case has the highest Nusselt and Reynolds numbers, whereas the SSC case has the lowest. The values of the FCC cases are in between those of SAC and SSC. In fact, they are close to the OB case. In general, heat and momentum transfer efficiencies of the fluid system are enhanced and decreased by increasing ϵ and D, respectively. As expected, the Nusselt number of both OB-like cases is close to that of the corresponding incompressible Rayleigh-Bénard case. The slight difference between the two can be accounted for by the fact that small, but non-negligible, compressibility effects are expected even when $\epsilon = D = 0.1$.

B. Structure of the superadiabatic temperature field

Although the mean values of the Nusselt and Reynolds numbers of FCC and OB are comparable, we observe significant differences in the contour plots of the superadiabatic temperature for all cases including FCC and OB in Figs. 1(b)–1(e). Figure 1(b) displays the OB-like dynamics with symmetric plume detachments from the boundary layers at top and bottom; the simulations of SAC in Fig. 1(c) develop a top-down asymmetry between falling and rising plumes, which will still not significantly alter the mean profiles across the layer, as we will see further below. Highly asymmetric configurations follow for FCC at the operating point (ϵ, D) close to the Mach number maximum M_f^* in Fig. 1(d) and for SSC with $D \to 1 - \epsilon$ where turbulence is strongly suppressed at the top and a clearly visible sublayer with reduced turbulence is formed; see Fig. 1(e). Except for the OB case, thinner plumes emanate from the top compared to those rising from the bottom. This is a general trait of compressibility regardless of the boundary layer thickness. Moreover, comparing the large D (FCC and SSC) cases, the stratified layer at the top becomes prominent for SSC at $D = 0.8$
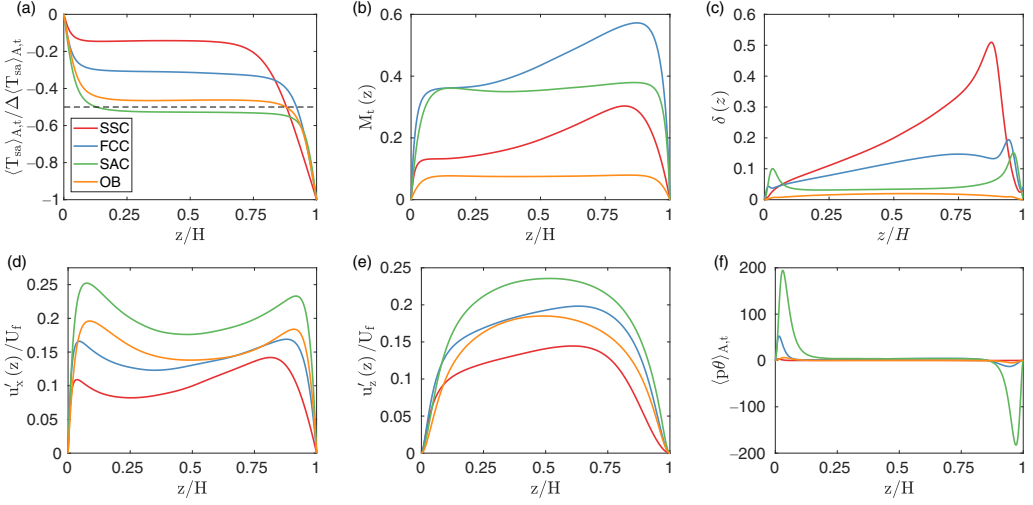
FIG. 3. Mean vertical profiles of plane-time averaged quantities as a function of superadiabaticity and dissipation number at Ra $\simeq 10^6$ (runs 5–8). We show (a) the normalized mean of the superadiabatic temperature $T_{sa}(z)$, (b) the turbulent Mach number $M_t(z)$, (c) the dilatation parameter $\delta(z)$, (d) the root-mean-square profiles of $u'_x(z)$ and (e) $u'_z(z)$, and, finally, (f) the mean of the pressure dilatation, $p\theta = p(\boldsymbol{\nabla} \cdot \boldsymbol{u})$. The color coding for all plots corresponds to the legend in (a). Data are for Ra $= 10^6$.

compared to FCC at $D = 0.5$. Also, the plumes which detach from the bottom in FCC get well mixed compared to those in SSC due to higher ϵ.

C. Vertical mean profiles and breakdown of top-down symmetry

The mean vertical profiles of the turbulence fields are summarized in Fig. 3. We recognize first that for most statistics, the FCC profiles are enclosed by those of the limit cases, SAC and SSC, which supports the idea of being a blend of these limits. Figure 3(a) shows the combined plane-time averages of the superadiabatic temperature T_{sa} renormalized by $\Delta_{sa} = \langle T_{sa}(0) \rangle_{A,t} - \langle T_{sa}(1) \rangle_{A,t}$ such that all four profiles are comparable. The OB-like and SAC cases with $D \ll 1$ give nearly symmetric profiles with a well-mixed bulk close to $\langle T_{sa} \rangle / \Delta_{sa} = 0.5$. In contrast, the cases FCC and SSC are characterized by significant offsets from the symmetric OB value of $\langle T_{sa}(z) \rangle_{A,t} = 0.5$. However, since ϵ and D are finite and not zero in the OB-like case (and thus the compressibility effects are present), we observe a small positive offset from a perfect top-down symmetry. In SAC, for which the superadiabaticity gets very large while D remains unchanged, the cold falling thinner plumes reach deeper into the bulk. This reverses the slight offset of the OB-like case into a negative one, $\langle T_{sa}(z) \rangle_{A,t} < 0.5$.

Mean vertical profiles of the *turbulent Mach number* M_t, defined as

$$M_t(z) = \frac{u'(z)}{\sqrt{\gamma R \langle T(z) \rangle_{A,t}}}, \tag{16}$$

are reported in Fig. 3(b). We again observe asymmetric curves for FCC and SSC, in agreement with those for the velocity fluctuations that will be discussed afterwards. The largest turbulent Mach numbers are found in FCC close to the top with values that remain consistently below the estimate, $\max_z[M_t(z)] < M_f^*$, from (6). The smallest values of $M_t(z)$ are observed for the OB-like regime. The estimate $M_f \leqslant 1$ in (6) was based on the bottom temperature T_{bot}. A free-fall Mach number based on the top plate temperature could alternatively be defined such that two free-fall Mach numbers are

obtained as a reference,

$$M_f^{\text{bot}} = M_f \quad \text{and} \quad M_f^{\text{top}} = \sqrt{\frac{\epsilon D}{(\gamma - 1)}} \sqrt{\frac{T_{\text{bot}}}{T_{\text{top}}}}. \tag{17}$$

For the FCC case, the free-fall Mach number with respect to the top is $M_f^{\text{top}} = 3.35$. Thus, in principle, supersonic conditions can exist at the top boundary; see, also, Ref. [25]. In Table I, we list the maximum (pointwise) turbulent Mach number $M_t^{\text{max}} = \max_{(\boldsymbol{x},t)} |\boldsymbol{u}(\boldsymbol{x},t)|/[\gamma RT(\boldsymbol{x},t)]^{1/2}$ obtained in our simulations for all cases. As expected, the highest maximum Mach number is for the FCC case around 1.32 for Ra $\approx 10^6$. Although supersonic, this is much lower than $M_f^{\text{top}} = 3.35$. This apparent discrepancy is because, near the top boundary, the velocities are negligible and the strongest velocity fluctuations are near the edge of the top boundary layer where the temperature, in turn, is higher than T_{top}. Indeed, we also see from Table I, for all cases, that M_t^{max} increases with the Rayleigh number (even though only two Ra values are available). Additional studies at higher Rayleigh numbers are thus required to understand the trend of compressibility effects with Rayleigh number.

In compressible turbulence, M_t alone cannot characterize the system. Donzis and Panickacheril John [49] showed that by including a further parameter—the *dilatation parameter* δ—along with M_t, universality for essential compressible statistics [50,51] was shown, and thus an easier systematic analysis of a compressible turbulent system is possible. Similar to Nu and Re, the parameters M_t and δ are the responses that show deviations from the Boussinesq regime, which are set by superadiabaticity ϵ and dissipation number D. In detail, the new parameter δ is given by

$$\delta = \frac{u_d'}{u_s'} \quad \text{with} \quad \mathbf{u} = \mathbf{u}_s + \mathbf{u}_d, \tag{18}$$

where the velocity field is subject to a Helmholtz decomposition into solenoidal and dilatational parts. Such decomposition is less straightforward in an inhomogeneous flow and works via the corresponding dissipation rates. We therefore assume the scaling of $\langle \epsilon_d \rangle / \langle \epsilon_s \rangle \propto \delta^2$, where $\langle \epsilon_d \rangle = 4\nu_0/3\langle(\nabla \cdot \mathbf{u})^2\rangle$ and $\langle \epsilon_s \rangle = \nu_0\langle\omega_i^2\rangle$ are the mean dilatational and solenoidal kinetic energy dissipation rates [52], respectively. Here, ω_i is the vorticity vector field and $\nu_0 = \mu_0/\rho_{\text{ref}}$ is the kinematic viscosity. For homogeneous flow, $\langle \epsilon_f \rangle = \langle \epsilon_s \rangle + \langle \epsilon_d \rangle$, but in our case, there will be inhomogeneous contributions to $\langle \epsilon_f \rangle$. However, even for our cases, the ratio of $\langle \epsilon_d \rangle / \langle \epsilon_s \rangle$ will give us a relative estimate of the dilatational motions between the different cases that we are considering here. Thus, we define

$$\delta(z) = \sqrt{\frac{\langle \epsilon_d(z) \rangle_{A,t}}{\langle \epsilon_s(z) \rangle_{A,t}}} = 2\sqrt{\frac{\langle(\nabla \cdot \mathbf{u})^2\rangle_{A,t}}{3\langle\omega_i^2\rangle_{A,t}}}. \tag{19}$$

In our context, $\delta(z)$ can be interpreted as the relative strength of kinetic energy dissipation due to shocklets or preshocks to that due to the vortical fluid motions. The higher δ, the larger fractions of acoustic motions in the flow field.

We show the variation of $\delta(z)$ in Fig. 3(c). Once again, the asymmetry between the top and bottom increases for growing D, with SSC being the case with dominant dilatational (or compressible) motion at the top boundary followed by the FCC case. For smaller D (in SAC and OB), the magnitude of the dilatational motions is more or less comparable at the top and bottom. Comparing the cases OB and SAC, the effect of superadiabaticity is to increase the strength of dilatational motions at both top and bottom in equal proportions. For high dissipation number D, i.e., the cases FCC and SSC, the parameter δ decreases monotonically from the top to the bottom in the bulk region of the convection layer.

The normalized profiles of the root mean squares of two velocity components are shown in Figs. 3(d) and 3(e). The profile of the horizontal component $u_x'(z)$ in Fig. 3(d) is qualitatively similar for all cases. The magnitude decreases with D, but increases with ϵ. The profiles of the y component

are similar and thus not shown. The vertical component $u_z'(z)$ is shown in Fig. 3(e). While the mean profiles are nearly symmetric for OB and SAC again, fluctuations are enhanced towards the top in the other two cases, FCC and SSC.

For compressible turbulence, the entropy is the conserved quantity rather than T_{sa}. Apart from temperature, there is an additional contribution to entropy from the pressure dilatation correlation, $p\theta$, where $\theta(\boldsymbol{x}) = \boldsymbol{\nabla} \cdot \boldsymbol{u}$ is the divergence of the velocity field. We plot $\langle p\theta \rangle_{A,t}$ in Fig. 3(f). One finds that this term is negligible for the OB and SSC cases, where $\epsilon \ll 1$. The pressure dilatation increases with ϵ, as seen for the FCC and SAC cases. However, significant variations are observed near the boundaries only and remain negligible in the bulk. This bulk behavior is, in fact, consistent with homogeneous isotropic compressible turbulence [53]. Although the magnitude of the instantaneous pressure dilatation fluctuations is considerably high, due to its oscillatory nature, the net contribution to the energy balance after averaging is negligibly small. The bulk behavior in convection is, to a certain extent, comparable to isotropic turbulence. Jones *et al.* [41] estimate a positive offset of T_{sa} in the bulk. However, empirical evidence from this study suggests that the offset of T_{sa} in the bulk remains small, as observed in Figs. 3(a) and 3(f).

D. Velocity field divergence

Figure 4(a) shows an instantaneous cut through $\theta(\boldsymbol{x}) = \boldsymbol{\nabla} \cdot \boldsymbol{u}$ for SAC, which corresponds to Fig. 1(c). Large regions of expansion ($\theta > 0$) are found near the bottom boundary, which corresponds to rising plumes. The expansive regions near the top boundary also correspond to falling plumes; however, they are surrounded by large regions of compression ($\theta < 0$) from the upward flow. The compression effect at the top is more pronounced since $\langle \rho(z) \rangle_{A,t}$ grows strongly for $z/H > 0.9$; see Figs. 4(c) and 4(d), where we plot the mean vertical profiles of the divergence $\theta(z) = \langle \boldsymbol{\nabla} \cdot \boldsymbol{u} \rangle_{A,t}$ and the density $\langle \rho(z) \rangle_{A,t}$. Maxima and minima of $\theta(z)$ are present in the bottom and top boundary layers, respectively. Moreover, since the directions x and y are homogeneous, $\theta(z) = \langle \boldsymbol{\nabla} \cdot \boldsymbol{u} \rangle_{A,t} = \langle \partial u_z / \partial z \rangle_{A,t}$. Note, also, that due to conservation of mass in our setup, $\int_0^1 \theta(z)dz = 0$; therefore, stronger compression at the top relative to expansion at the bottom results in a thinner top boundary layer.

The SAC limit is consequently weakly top-down asymmetric only. The asymmetry of the SAC case towards the top boundary [see Fig. 3(a)] can be partially explained as follows. Along with constant dynamic viscosity μ_0 and thermal conductivity k_0, the high and low density at the top and bottom results in low and high kinematic viscosity $\nu = \mu_0/\rho$ and thermal diffusivity $\kappa = k_0/(c_p\rho)$, respectively. Similar to incompressible convection, this can lead to a thinner boundary layer at the top for the fluid with a higher density. However, in SAC, strong compressible mechanisms lead to these strong density variations.

We conclude that the stronger asymmetry of boundary layers in the FCC case (see Fig. 3)—the blend of SAC and SSC—have to be traced back mainly to the SSC limit, which is further detailed in Fig. 4(b). In this regime, the mass balance can be simplified to the anelastic case for sufficiently small ϵ, $\boldsymbol{\nabla} \cdot (\bar{\rho}\boldsymbol{u}) \approx 0$ [39]. (Strictly speaking, this relation is only valid for $M_t \ll 1$, which is not the case for the present SSC case near the top boundary. The specific implications of the high compressibility for $0.9 < z/H < 1$ were analyzed in [47] and will be briefly discussed in the final section. For most of the convection domain, anelasticity can be assumed in the SSC case.) With a monotonically decreasing adiabatic profile $\bar{\rho}(z)$, this leads to a pointwise relation of

$$\boldsymbol{\nabla} \cdot \boldsymbol{u} = \boldsymbol{\nabla}_h \cdot \boldsymbol{u}_h + \frac{\partial u_z}{\partial z} \approx \left| \frac{d\bar{\rho}}{dz} \right| \frac{u_z}{\bar{\rho}} . \tag{20}$$

Generally, any up- and downwelling plume should expand and compress, respectively. Depending on the sign of $\partial u_z / \partial z$, one gets structures which are different from the incompressible case. Close to the bottom, SSC has $u_z > 0$ in plume detachment zones and thus $\theta(\boldsymbol{x}) > 0$ by Eq. (20) since $\rho > 0$. The horizontal velocity $\boldsymbol{u}_h$, which converges to these detachment regions, is weaker and thus less strictly converging as in the incompressible case. This leads to broader regions with accelerated
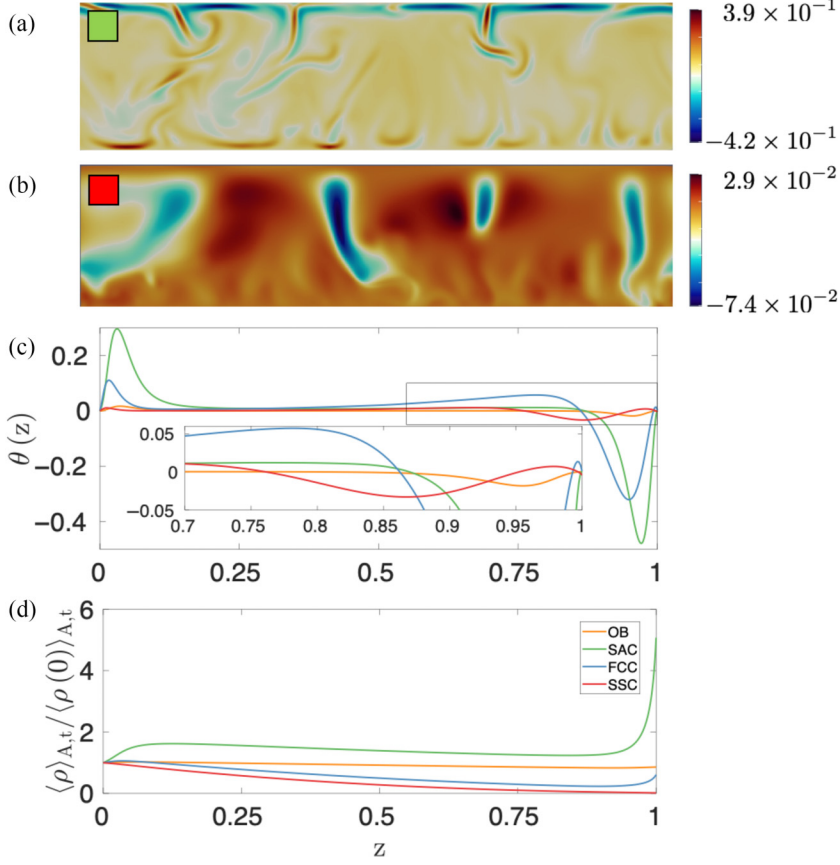
FIG. 4. Velocity divergence and mass density analysis. Instantaneous vertical cut of $\nabla \cdot \boldsymbol{u}$ for (a) strongly superadiabatic case (SAC), which corresponds to the snapshot in Fig. 1(c), and (b) strongly stratified case (SSC), which corresponds to Fig. 1(f). (c) Mean vertical profiles of $\theta(z) = \langle \nabla \cdot \boldsymbol{u} \rangle_{A,t}$. The inset magnifies the profiles close to the top wall, as indicated by the box in the main panel. (d) Mean vertical mass density profiles. Again, Ra $\simeq 10^6$ and Pr $= 0.7$ in all cases. Line styles in (c) and (d) are identical to Fig. 3.

upward flow, $\partial u_z/\partial z > 0$, compared to incompressible convection. It is clear from Fig. 4(b) that the bottom boundary is dominated by expansions with $\theta(\boldsymbol{x}) > 0$ and $u_z > 0$, which results in a positive $\theta(z)$ near the bottom. The figure also shows that a positive velocity field divergence fills nearly the whole bulk, interrupted only by a negative one with a significantly higher magnitude in the narrow downward plume regions. It can be expected that this contrast (which leads to a net zero mean, as seen in the mean profiles) increases for $D \to 1 - \epsilon$; see, also, a discussion in Spruit [48] in the solar context. This is not clear in Fig. 4(c) since the magnitude of $\theta(\boldsymbol{x})$ for SAC and FCC with their larger ϵ is greater than in SSC. Qualitatively, the bottom boundary dynamics of SAC and SSC is similar.

At the top, following from Fig. 4(c) (see, also, the inset), we get $\theta(z) < 0$ for $0.6 \lesssim z/H \lesssim 0.9$, except directly near the wall for $z/H \gtrsim 0.9$. Here, $\theta(z) < 0$ implies upward decelerating plumes coming from the bottom, similar to SAC. This broadly upwelling fluid is increasingly compressed, which leads to $d\langle \rho_{\mathrm{sa}} \rangle_{A,t}/dz > 0$ for $0.6 \lesssim z \lesssim 0.9$ with $\rho_{\mathrm{sa}} = \rho - \bar{\rho}(z)$ (not shown). However, for SSC with its strong stratification, the plumes can no longer reach the top boundary. From Figs. 4(b) and 4(c), it is clear that the magnitudes of $\theta(z)$ and $\theta(\boldsymbol{x})$ in the layer $0.9 \lesssim z/H \lesssim 1.0$ are smaller than for $0.6 \lesssim z/H \lesssim 0.9$. The near-wall layer corresponds to very weak fluid motion due to high stratification. Here, thermal plumes detach from the top wall and get increasingly focused when

shooting downwards deep into the bulk, in agreement with (20). As seen from Figs. 4(b) and 1(f), these downward-directed plumes always correspond to a negative divergence. This is in contrast to SAC, where the downwelling thermal plumes effectively expand even though they are compressed in the horizontal directions.

Comparing Figs. 1(d) with 4(a) and Figs. 1(f) with 4(b) for SAC and SSC, respectively, we observe a one-to-one correspondence between thermal plumes from the top in T_{sa} and high-magnitude regions of θ. This suggests genuine compressibility effects on the top boundary.

For the SSC case in Fig. 4(d), the density near the bottom is large compared to the top, which would imply a higher Rayleigh number near the bottom. However, we observe thinner plumes from the top boundary due to compressibility. Thus, high compressibility plays a significant role in plume formation and structure. The background stratification of density is observed in the bulk region for all four cases; see Table I. This is, of course, most obvious for the cases with high D, i.e., the SSC ($D = 0.8$) and FCC ($D = 0.5$) cases. The superadiabaticity ϵ is a measure of departure from the equilibrium adiabatic profile. Thus, for the OB and SSC cases, where $\epsilon = 0.1$, the departure from the adiabatic profile is not apparent. A significant departure from the adiabatic profile is seen for the SAC case at both of the boundaries with $\epsilon = 0.8$ and $D = 0.1$. Positive and negative density gradients towards the wall are observed at the top and bottom boundaries respectively. They correspond to unstable convective configurations. Thus, as expected, for the SAC case, the high superadiabaticity of $\epsilon = 0.8$ easily overcomes the weak background stratification, which corresponds to $D = 0.1$. Consistent with thinner plume structures seen in Figs. 1(c) and 4(a) at the top boundary, high-density gradients are observed for the top boundary relative to the bottom one. For the FCC case with $D = 0.5$, moderate stratification of the density is seen across the bulk. The behavior near the top boundary is similar to the SAC case with a positive density gradient due to moderate $\epsilon = 0.45$. However, it is not high enough to observe departures from the adiabatic profile near the bottom boundary.

E. Local thermal boundary layer thickness.

The strong asymmetry between the boundary layer (BL) dynamics at the top and bottom and the suppression of fluctuations in the SSC case is finally verified by the distribution of the *local thermal boundary layer thickness*, which is given in dimensionless and renormalized form by [cf. [31] and compare with Eq. (12)]

$$\lambda_T^{bot,top} = |\langle T_{sa}(0, 1) - T_{sa}(0.5)\rangle_{A,t}| \left|\frac{\partial T_{sa}}{\partial z}\right|^{-1}_{z/H=0,1}. \tag{21}$$

Figure 5 shows the probability density functions (PDFs) of the local thickness evaluated for the four cases at Ra $\simeq 10^6$. It is seen that the distributions at the bottom plane collapse fairly well in the core. Extended left tails are observed for FCC and SSC, which also generate the thinnest local BL thicknesses. At the top, the differences between the runs are more significant. While both distributions agree well for the OB-like case (and thus only the bottom PDF is shown), those of the other cases deviate increasingly, most strongly for SSC. The latter distribution is characterized by a small variance and peaked at large local thickness; see, also, Fig. 1(a). Quantitatively, the discrepancy between the PDFs at the top and bottom can be determined by the Kullback-Leibler (KL) divergence [30], which is given by

$$KL[p^{top} \parallel p^{bot}] = \sum_{i=1}^{N_p} p_i^{top} \ln\left(\frac{p_i^{top}}{p_i^{bot}}\right), \tag{22}$$

with $p^{top} = p(\lambda_T^{top})$ and $p^{bot} = p(\lambda_T^{bot})$. The index i runs over the bins of both PDFs, and N_p is the total number of bins. The inset of Fig. 5(b) shows the KL divergence and detects an increasing deviation of both PDFs, which is strongest for the SSC case.
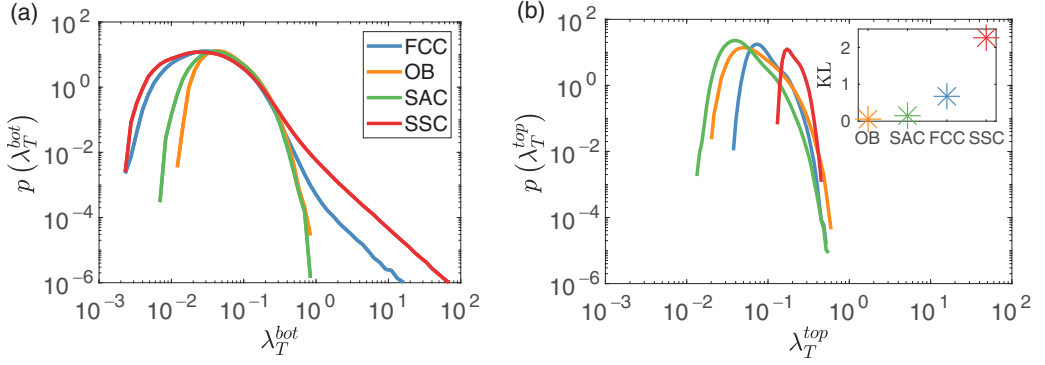
FIG. 5. Probability density functions of the local thermal boundary layer thickness at the (a) bottom and (b) top. The inset in (b) displays the Kullback-Leibler divergence (KL) for the four runs at Ra $\approx 10^6$.

VI. COMPRESSIBILITY IN THE MACH NUMBER–DILATATION PARAMETER PLANE

In compressible turbulence, it is well known that the system cannot be characterized by the turbulent Mach number alone, but also depends on the external driving conditions. Recently, Donzis and Panickacheril John [49] showed that by including the dilatation parameter δ along with M_t, for a variety of driving conditions, at least for homogeneous compressible turbulence, the universality for many statistical properties can be demonstrated in terms of these two parameters. Thus, the behavior of compressible turbulence crucially depends on where the system is in the M_t–δ phase plane.

Even though the extension of the ideas from Ref. [49] to inhomogeneous flows is not fully understood or studied, recent investigations [37,54] demonstrate that the Mach number along with the dilatation parameter are again required to characterize heat flux at the boundaries in compressible turbulent channel flows for different thermal boundary conditions. We stress that we assume $\langle \epsilon_d \rangle / \langle \epsilon_s \rangle \propto \delta^2$ with a proportionality constant $O(1)$ to arrive at the definition of δ in (19). Consequently, we only get a relative estimate of the compressibility conditions across the layer depth for the four different cases. Thus comparing our data in the M_t–δ phase plane will give us a first-order estimate of the compressibility conditions in the convection flows.

To this end, we combine the data from Figs. 3(b) and 3(c) in the new Fig. 6 to represent the variation of $\delta(z)$ and $M_t(z)$ for all four cases in the phase plane. In all panels, the circles and squares correspond to the location of the maximum M_t near the top and bottom boundary, respectively. These locations are considered to be the edge of the viscous or thermal boundary layer. The diamonds stand for the midsection of the layer. The solid and dashed lines correspond to the points inside the bottom and top boundary, respectively. The bulk region is considered to be between the circles and squares.

We see that $M_t \approx 0$ very close to the wall for all cases. However, here we find that except for the OB case in Fig. 6(a), δ has a finite value near the boundaries. The black-dotted line in all the figures is the equipartition line, $f_{eq} = \delta \sqrt{\delta^2 + 1}/M_t = 0.5$, from Donzis and Panickacheril John [49]. This line demarcates two different regimes of compressible turbulence in homogeneous isotropic turbulence. In the $f_{eq} < 0.5$, the solenoidal or incompressible nature of pressure dominates over the acoustic or dilatational nature. For $f_{eq} > 0.5$, the acoustic pressure starts to dominate over the solenoidal pressure and it is called weak equipartition regime.

From Fig. 6(a), one observes that for the OB case, both the top and bottom boundaries almost overlap each other perfectly in the phase plane, implying a nearly perfect top-down symmetry of both boundary layer. For the SAC case Fig. 6(b), very close to the wall, unlike the OB case, the top and bottom boundaries do not overlap, but are close to each other. This again is consistent with the slight asymmetry seen for the SAC case in Fig. 5. Similar to Fig. 5, an increase of D is connected with increasing differences in the phase plane, as visible for the cases FCC and SSC in Figs. 6(c)
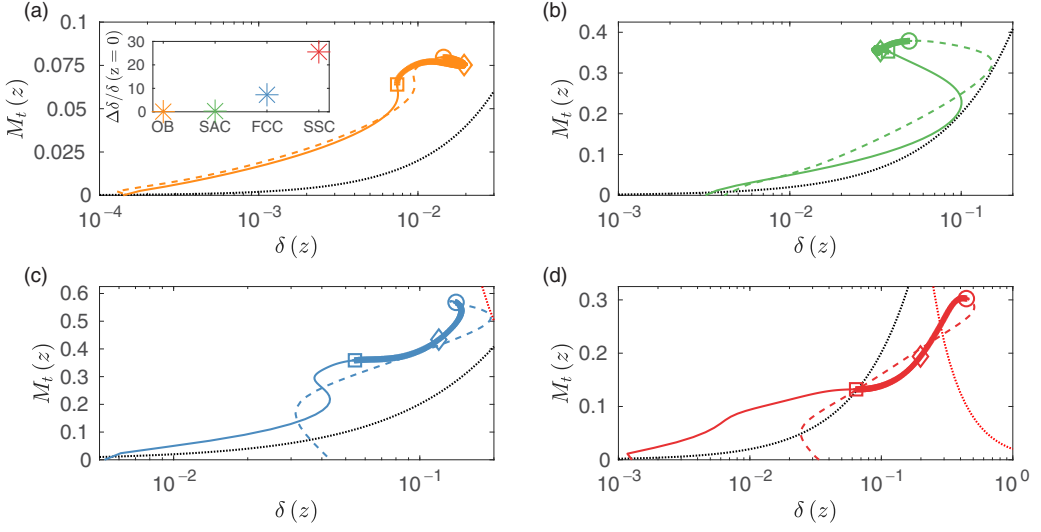
FIG. 6. Compressible convection regimes in M_t–δ phase plane for Ra $\approx 10^6$ (runs 5–8). The data for $M_t(z)$ and $\delta(z)$ are taken from Figs. 3(b) and 3(c), respectively. (a) Case OB, (b) case SAC, (c) case FCC, and (d) case SSC. The hollow circles and squares for all cases correspond to the location of maximum M_t near the top and bottom boundaries. The diamonds correspond to the layer center. The region between the square and circle is considered as the bulk and marked by crosses. The top boundary layer region between the top wall and the circle is shown as a dashed line in each panel. Similarly, the solid line corresponds to the bottom boundary layer region between the bottom boundary and the square. The dotted black and red lines in all figures correspond to the equipartition line ($f_{eq} = \delta\sqrt{\delta^2 + 1}/M_t = 0.5$) and a skewness line ($\delta^2 M_t = 0.025$), respectively [49]. The inset of (a) shows the ratio $\Delta\delta/\delta(z = 0)$ near the regions between the top and bottom walls for the four cases.

and 6(d), respectively. For the SSC case, very near the wall, the difference between the curves for the top and bottom boundary is strongest.

Moreover, we notice that if the estimate of f_{eq} for homogeneous flows is also valid for the present inhomogeneous system, then the top and bottom boundary layers of SSC would be found in different regimes of compressible turbulence. One can quantify the difference with the measure, $\Delta\delta/\delta(z = 0)$, where $\Delta\delta = \delta(z = H) - \delta(z = 0)$. We plot this measure as an inset in Fig. 6(a) for all four cases. A striking similarity between $\Delta\delta/\delta(z = 0)$ and the KL divergence is found. Clearly, this indicates that the relative strength of the dilatational motions plays an important role in the boundary layer dynamics of compressible convection. Finally, we notice that for the low-D cases SAC and OB, the variability of compressibility conditions in the phase plane is very limited, implying homogeneity across the bulk. In fact, for the SAC, this range is the most narrow one. The opposite trend is observed as the dissipation number D increases, which indicates an inefficiency of the turbulent mixing.

VII. DETAILED ENERGY BUDGET ANALYSIS

The energy balance equation (1c) can also be written as

$$C_p \frac{\partial(\rho T)}{\partial t} + C_p \frac{\partial(\rho u_j T)}{\partial x_j} - \frac{\partial p}{\partial t} - u_j \frac{\partial p}{\partial x_j} = \frac{\partial}{\partial x_j}\left(k \frac{\partial T}{\partial x_j}\right) + \sigma_{ij} S_{ij}. \tag{23a}$$

Averaging over horizontal planes and time, along with the assumption of a statistically steady state, we get

$$C_p \frac{\partial \langle \rho u_j T \rangle_{A,t}}{\partial x_j} - \left\langle u_j \frac{\partial p}{\partial x_j} \right\rangle_{A,t} = \frac{\partial}{\partial x_j} \left\langle k \frac{\partial T}{\partial x_j} \right\rangle_{A,t} + \langle \sigma_{ij} S_{ij} \rangle_{A,t}. \tag{23b}$$

Since we have homogeneity in both horizontal directions, the equation can further be simplified to

$$C_p \frac{d \langle \rho u_z T \rangle_{A,t}}{dz} - \left\langle u_j \frac{\partial p}{\partial x_j} \right\rangle_{A,t} = \frac{d}{dz} \left\langle k \frac{dT_{\mathrm{sa}}}{dz} \right\rangle_{A,t} + \langle \sigma_{ij} S_{ij} \rangle_{A,t}. \tag{23c}$$

Note that we have also replaced T with the superadiabatic temperature T_{sa} since the adiabatic temperature profile, $\overline{T}(z) = T_{\mathrm{bot}}(1 - Dz)$, is a linear function of z. Finally, integrating from the bottom wall to an arbitrary z, we get

$$C_p \langle \rho u_z T \rangle_{A,t}(z) - \left\langle k \frac{dT_{\mathrm{sa}}}{dz} \right\rangle_{A,t}(z) - \int_0^z \left\langle u_j \frac{\partial p}{\partial x_j} \right\rangle_{A,t} dz' - \int_0^z \langle \sigma_{ij} S_{ij} \rangle_{A,t}(z') dz' = \text{const.} \tag{23d}$$

For the OB Rayleigh-Bénard convection case, the contribution from the last two terms constituting the compression work and energy dissipation, respectively, is negligible. After normalizing with $k_0 \Delta T / (C_p \rho_{\mathrm{ref}} H)$, one would get the standard Nusselt number definition [4],

$$\mathrm{Nu}(z) = \frac{\langle u_z T \rangle_{A,t}(z) - \frac{k_0}{C_p \rho_{\mathrm{ref}}} \left\langle \frac{dT_{\mathrm{sa}}}{dz} \right\rangle_{A,t}(z)}{\frac{k_0}{C_p \rho_{\mathrm{ref}}} \frac{\Delta T}{H}}, \tag{24}$$

which has to be constant for each horizontal plane $0 \leqslant z \leqslant H$. Normalizing Eq. (23d) with $\epsilon T_{\mathrm{bot}} k / H$, one gets

$$\underbrace{\left[\frac{C_p H}{k \epsilon T_{\mathrm{bot}}} \right] \langle \rho u_z T \rangle_{A,t}}_{=J_c(z)} - \underbrace{\left[\frac{H}{k \epsilon T_{\mathrm{bot}}} \right] \int_0^z \left\langle u_j \frac{\partial p}{\partial x_j} \right\rangle_{A,t} dz'}_{=J_p(z)} - \underbrace{\left[\frac{H}{\epsilon T_{\mathrm{bot}}} \right] \left\langle \frac{dT_{\mathrm{sa}}}{dz} \right\rangle_{A,t}}_{=J_d(z)} - \underbrace{\left[\frac{H}{k \epsilon T_{\mathrm{bot}}} \right] \int_0^z \langle \sigma_{ij} S_{ij} \rangle_{A,t} dz'}_{=J_{\langle \epsilon \rangle}(z)}$$

$$= \text{const.} \tag{25}$$

Equation (25) contains the diffusive current $J_d(z)$ at the boundaries $z = 0$ and H; the other terms vanish due to the no-slip boundary conditions for the velocity field. This confirms our definition of the Nusselt number in (14). In Eq. (25), the terms $J_c(z), J_p(z), J_d(z)$, and $J_{\langle \epsilon \rangle}(z)$ denote the convective heat current, the current due to compression work, the diffusive heat current, and energy dissipation current, respectively. We plot these fluxes and their partial and total sums as a function of depth z for all four convection cases in Fig. 7 at $\mathrm{Ra} = 10^6$. The sum of all these terms is a constant, i.e.,

$$\mathrm{Nu}(z) = J_{\mathrm{tot}}(z) = J_c(z) + J_p(z) + J_d(z) + J_{\langle \epsilon \rangle}(z) = \mathrm{Nu}. \tag{26}$$

See, again, Table I for the Nusselt number of all cases.

In Figs. 7(a) and 7(b), the compression work and dissipation terms perfectly cancel each other over the entire domain, and thus the relation has to be very close to the exact Rayleigh-Bénard case, $J_c + J_d = \mathrm{Nu}$. For the SAC case, due to high superadiabaticity with $\epsilon = 0.8$, the magnitude of these two canceling terms increases with height.

For the cases FCC and SSC in Figs. 7(c) and 7(d), significant differences are observed. The sum $J_p(z) + J_{\langle \epsilon \rangle}(z) \neq 0$ across the domain. Also, the magnitude of both terms is significantly higher. Since the diffusive flux $J_d \approx 0$ in the bulk, the difference between the J_p and J_d has to be compensated by J_c. Thus, unlike the incompressible Rayleigh-Bénard case, $J_c \geqslant \mathrm{Nu}$ rather than $J_c = \mathrm{Nu}$ in the bulk. In other words, a fraction of the convective current in the bulk is used for balancing between the compression work and dissipation contributions, which might explain the decreased amount of transported heat for the higher-D cases.
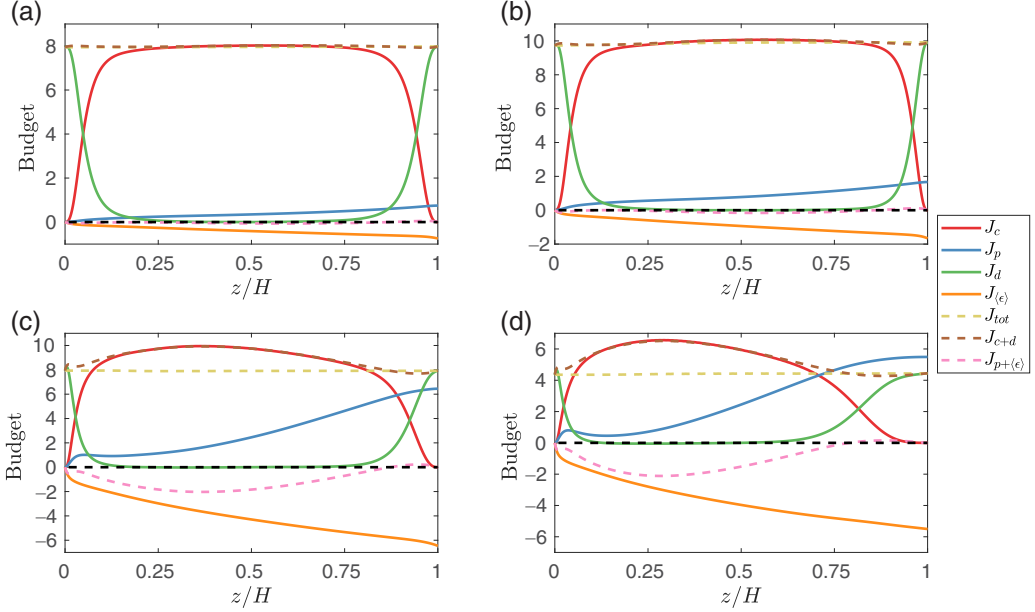
FIG. 7. Detailed energy budget vs layer height for all four convection cases. (a) Case OB, (b) case SAC, (c) case FCC, and (d) case SSC. The definitions of the fluxes J_c, J_d, J_p, and $J_{\langle\epsilon\rangle}$ are given in Sec. VII. We also show $J_{\text{tot}} = J_c + J_p + J_d + J_{\langle\epsilon\rangle}$, and the partial sums $J_{c+d} = J_c + J_d$ and $J_{p+\langle\epsilon\rangle} = J_p + J_{\langle\epsilon\rangle}$. All data are again for Ra $= 10^6$. Note that in (a) and (b), the flux J_{tot} practically coincides with J_{c+d}.

VIII. FINAL DISCUSSION

The central objective of this work was a systematic exploration of different regimes of fully compressible convection which are determined by the superadiabaticity ϵ and the dissipation number D. For sufficiently large amplitudes of both parameters, convection proceeds beyond the Oberbeck-Boussinesq and anelastic limits. We focused on genuine compressibility effects and excluded other non-Oberbeck-Boussinesq contributions which can arise from complicated dependencies of the material parameters, such as of the dynamic viscosity or the thermal conductivity on the thermodynamic state variables T and p. We identified three limiting cases in the three corners of the triangular parameter plane, which is spanned by superadiabaticity and dissipation number. These are the Oberbeck-Boussinnesq-like limit for $\epsilon \ll 1$ and $D \ll 1$, the strongly superadiabatic convection case for $\epsilon \to 1$ and $D \ll 1$, and the strongly stratified convection case for $\epsilon \ll 1$ and $D \to 1$. A fourth regime maximizes the Mach number and can be considered as a blend of the latter two regimes with $\epsilon \sim D \sim 0.5$.

We have systematically explored the mean profiles of central quantities, such as the temperature, the velocity fluctuations, or the convective heat flux. A further aspect of the present study was to transfer the analysis concepts from homogeneous, isotropic compressible turbulence to the present flow with one inhomogeneous spatial direction, e.g., by monitoring the turbulent Mach number and dilatation parameter in the phase plane; see Fig. 6.

The majority of convection problems are discussed either in the Oberbeck-Boussinesq or the anelastic approximations. These approximations can be well described in terms of the asymptotic limits of ϵ and D. The Oberbeck-Boussinesq approximation corresponds to $\epsilon \to 0$ and, subsequently, $D \to 0$. The anelastic approximation stands $\epsilon \to 0$ and a finite D, such that the Mach number $M_f \to 0$. Other low-Mach-number approximations [42–44] have been proposed in the literature. These approximations are less restrictive compared to the anelastic one. Unlike the AE approximation, these models allow for large variations of density and temperature about their

mean values. However, pressure fluctuations are neglected. Where would these low-Mach-number approximations be found in the $\epsilon - D$ phase plane? On the one hand, they should be valid in the anelastic limit; on the other hand, they should be valid in the limit of vanishing D with a finite superadiabaticity ϵ. The finite ϵ allows for large variations of density and temperature. However, $D \to 0$, and thus $M_f \to 0$, implies that that the pressure variations are negligible. All our simulations have a considerable Mach number near the top boundary; thus these approximations are not valid.

Of particular interest from our point of view is the SSC case. Highly top-down-asymmetric compressible convection is obtained for the strong stratification case, i.e., for $D \to 1 - \epsilon$. In this regime, we detect a sublayer with strongly reduced velocity, temperature fluctuations, and a reduced convective heat flux. These properties are also documented by the resulting Nusselt and Reynolds numbers in Table I. Out of this layer, self-focusing thermal plumes are ejected deep into the bulk of the strongly stratified convection zone. A focusing effect in compressible turbulence has been recently reported in laboratory experiments by Manzano *et al.* [55].

Even though our compressible convection simulations, which do not include magnetic fields and radiation transfer, are certainly much simpler than stellar convection flows, they might provide interesting new insights on how the heat is transported by nonlocal coherent downwelling plumes that detach from the top boundary layer. As suggested in the review of Spruit [48], this might be particularly important when strong density stratification exists and the level of turbulence is strongly reduced in regions between the downwelling plumes. The latter point might be connected to the solar conundrum in the upper solar convection zone, which reports anomalously weak velocity fluctuations for depths $z \gtrsim 0.92 R_\odot$, determined by helioseismology [32]. We thus think that our present DNS, in particular those in the SSC regime, might provide an interesting testing bed for the exploration of some basic processes and concepts in such flows, e.g., the formation of these plumes and their turbulence production by shear instabilities. Indeed, estimated dissipation numbers D would be significant when using data from model S of the solar interior [24,56]: (1) If we take the surface layer with a depth of 0.01 $R_\odot$, which corresponds to $H \approx 6900$ km, we have $T_{\mathrm{bot}} \simeq 4.6 \times 10^4$ K, $g \simeq 290$ m/s^2, $c_p \simeq 4.7 \times 10^4$ J/(kg K). This results in $D \approx 0.93$. (2) If we would take the lower half of the convection zone as a convection layer which corresponds to $H \approx 10^5$ km, we have $T_{\mathrm{bot}} \simeq 2.2 \times 10^6$ K, $g \simeq 430$ m/s^2, $c_p \simeq 3.5 \times 10^4$ J/(kg K). This results in a much smaller dissipation number of $D \approx 0.56$. Note that the values for g and c_p have been estimated as geometric means with three reference points for this coarse estimate.

Motivated by this discussion, we will continue to explore the highly stratified regime at higher Rayleigh and lower Prandtl numbers in the future.

[1] L. P. Kadanoff, Turbulent heat flow: Structures and scaling, Phys. Today **54**(8), 34 (2001).

[2] E. D. Siggia, High Rayleigh number convection, Annu. Rev. Fluid Mech. **26**, 137 (1994).

[3] G. Ahlers, S. Grossmann, and D. Lohse, Heat transfer and large scale dynamics in turbulent Rayleigh-Bénard convection, Rev. Mod. Phys. **81**, 503 (2009).

[4] F. Chillà and J. Schumacher, New perspectives in turbulent Rayleigh-Bénard convection, Eur. Phys. J. E **35**, 58 (2012).

[5] M. K. Verma, *Physics of Buoyant Flows* (World Scientific, Singapore, 2018).

[6] B. Stevens, Atmospheric moist convection, Annu. Rev. Earth Planet. Sci. **33**, 605 (2005).

[7] O. Pauluis and J. Schumacher, Self-aggregation of clouds in conditionally unstable moist convection, Proc. Natl. Acad. Sci. USA **108**, 12623 (2011).

[8] J. P. Mellado, Cloud-top entrainment in stratocumulus clouds, Annu. Rev. Fluid Mech. **49**, 145 (2017).

[9] P. Urban, P. Hanzelka, T. Králík, V. Musilová, A. Srnka, and L. Skrbek, Effect of boundary layers asymmetry on heat transfer efficiency in turbulent Rayleigh-Bénard convection at very high Rayleigh numbers, Phys. Rev. Lett. **109**, 154301 (2012).

[10] L.-A. Couston, D. Lecoanet, B. Favier, and M. Le Bars, Dynamics of mixed convective–stably-stratified fluids, Phys. Rev. Fluids **2**, 094804 (2017).

[11] S. Toppaladoddi and J. S. Wettlaufer, Penetrative convection at high Rayleigh numbers, Phys. Rev. Fluids **3**, 043501 (2018).

[12] A. Pandey, J. Schumacher, and K. R. Sreenivasan, Non-Boussinesq low-Prandtl-number convection with a temperature-dependent thermal diffusivity, Astrophys. J. **907**, 56 (2021).

[13] A. Pandey, J. Schumacher, and K. R. Sreenivasan, Non-Boussinesq convection at low Prandtl numbers relevant to the Sun, Phys. Rev. Fluids **6**, 100503 (2021).

[14] I. L. Pioro and B. Romney, *Woodhead Publishing Series in Energy: Handbook of Generation IV Nuclear Reactors* (Woodhead Publishing, Sawston, UK, 2016).

[15] J. Fröhlich, P. Laure, and R. Peyret, Large departures from Boussinesq approximation in the Rayleigh-Bénard problem, Phys. Fluids A **4**, 1355 (1992).

[16] C. A. Jones and K. M. Kuzanyan, Compressible convection in the deep atmospheres of giant planets, Icarus **204**, 227 (2009).

[17] T. Gastine and J. Wicht, Effects of compressibility on driving zonal flow in gas giants, Icarus **219**, 428 (2012).

[18] K. A. Emmanuel, An air-sea interaction theory for tropical cyclones. Part 1, J. Atmos. Sci. **43**, 585 (1986).

[19] L. Renault, J. C. McWilliams, and S. Masson, Satellite observations of imprint of oceanic current on wind stress by air-sea coupling, Sci. Rep. **7**, 17747 (2017).

[20] S. R. Lantz and Y. Fan, Anelastic magnetohydrodynamic equations for modeling solar and stellar convection zones, Astrophys. J. Suppl. **121**, 247 (1999).

[21] R. F. Stein, Solar surface magneto-convection, Living Rev. Solar Phys. **9**, 4 (2012).

[22] F. Rincon and M. Rieutord, The Sun's supergranulation, Living Rev. Solar Phys. **15**, 6 (2018).

[23] A. Brandenburg, Stellar mixing length theory with entropy rain, Astrophys. J. **832**, 6 (2016).

[24] J. Schumacher and K. R. Sreenivasan, Colloquium: Unusual dynamics of convection in the Sun, Rev. Mod. Phys. **92**, 041001 (2020).

[25] F. Cattaneo, N. E. Hurlburt, and J. Toomre, Supersonic convection, Astrophys. J. **349**, L63 (1990).

[26] A. Malagoli, F. Cattaneo, and N. H. Brummell, Turbulent supersonic convection in three dimensions, Astrophys. J. **361**, L33 (1990).

[27] C. Federath, R. S. Klessen, L. Iapichino, and J. R. Beattie, The sonic scale of interstellar turbulence, Nat. Astron. **5**, 365 (2021).

[28] W. Sutherland, The viscosity of gases and molecular force, London Edinburgh Dublin Philos. Mag. J. Sci. **36**, 507 (1893).

[29] S. Horn, O. Shishkina, and C. Wagner, On non-Oberbeck–Boussinesq effects in three-dimensional Rayleigh–Bénard convection in glycerol, J. Fluid Mech. **724**, 175 (2013).

[30] I. Goodfellow, Y. Bengio, and A. Courville, *Deep Learning* (MIT Press, Cambridge, MA, 2016).

[31] J. D. Scheel and J. Schumacher, Local boundary layer scales in turbulent Rayleigh-Bénard convection, J. Fluid Mech. **758**, 344 (2014).

[32] S. M. Hanasoge, Jr., T. L. Duvall, Jr., and K. R. Sreenivasan, Anomalously weak solar convection, Proc. Natl. Acad. Sci. USA **109**, 11928 (2012).

[33] S. K. Lele, Compact finite difference schemes with spectral like resolution, J. Comput. Phys. **103**, 16 (1992).

[34] S. Jagannathan and D. A. Donzis, Reynolds and Mach number scaling in solenoidally-forced compressible turbulence using high-resolution direct numerical simulations, J. Fluid Mech. **789**, 669 (2016).

[35] K. Kumari and D. A. Donzis, Direct numerical simulations of turbulent flows using high-order asynchrony-tolerant schemes: Accuracy and performance, J. Comput. Phys. **419**, 109626 (2020).

[36] S. Pirozzoli, Numerical methods for high-speed flows, Annu. Rev. Fluid Mech. **43**, 163 (2011).

[37] A. Baranwal, D. A. Donzis, and R. D. W. Bowersox, Asymptotic behaviour at the wall in compressible turbulent channels, J. Fluid Mech. **933**, A28 (2022).

[38] J. D. Scheel, M. S. Emran, and J. Schumacher, Resolving the fine-scale structure in turbulent Rayleigh-Bénard convection, New J. Phys. **15**, 113063 (2013).

[39] J. Verhoeven, T. Wiesehöfer, and S. Stellmach, Anelastic versus fully compressible turbulent Rayleigh-Bénard convection, Astrophys. J. **805**, 62 (2015).

[40] T. Alboussière and Y. Ricard, Rayleigh-Bénard stability and the validity of quasi-Boussinesq or quasi-anelastic liquid approximations, J. Fluid Mech. **817**, 264 (2017).

[41] C. A. Jones, K. A. Mizerski, and M. Kessar, Fully developed anelastic convection with no-slip boundaries, J. Fluid Mech. **930**, A13 (2022).

[42] D. R. Durran, Improving the anelastic approximation, J. Atmos. Sci. **46**, 1453 (1989).

[43] R. Klein and O. Pauluis, Thermodynamic consistency of a pseudoincompressible approximation for general equations of state, J. Atmos. Sci. **69**, 961 (2012).

[44] A. S. Almgren, J. B. Bell, C. A. Rendleman and M. Zingale, Low Mach number modeling of type Ia supernovae. I. Hydrodynamics, Astrophys. J. **637**, 922 (2006).

[45] Y. Ogura and N. A. Phillips, Scale analysis of deep and shallow convection in the atmosphere, J. Atmos. Sci. **19**, 173 (1962).

[46] F. Cattaneo, N. H. Brummell, J. Toomre, A. Malagoli and N. E. Hurlburt, Turbulent compressible convection, Astrophys. J. **370**, 282 (1991).

[47] J. Panickacheril John and J. Schumacher, Compressible turbulent convection in highly stratified adiabatic background, J. Fluid Mech. **972**, R4 (2023).

[48] H. C. Spruit, Convection in stellar envelopes: A changing paradigm, Mem. Soc. Astron. Ital. **68**, 397 (1997).

[49] D. A. Donzis and J. Panickacheril John, Universality and scaling in homogeneous compressible turbulence, Phys. Rev. Fluids **5**, 084609 (2020).

[50] J. Panickacheril John, D. A. Donzis, and K. R. Sreenivasan, Solenoidal scaling laws for compressible mixing, Phys. Rev. Lett. **123**, 224501 (2019).

[51] J. Panickacheril John, D. A. Donzis, and K. R. Sreenivasan, Does dissipative anomaly hold for compressible turbulence? J. Fluid Mech. **920**, A20 (2021).

[52] S. Sarkar, G. Erlebacher, M. Y. Hussaini, and H. O. Kreiss, The analysis and modeling of dilatational terms in compressible turbulence, J. Fluid Mech. **227**, 473 (1991).

[53] S. Sarkar, The pressure-dilatation correlation in compressible flows, Phys. Fluids A **4**, 2674 (1992).

[54] A. Baranwal and D. A. Donzis, and R. D. Bowersox, Turbulent heat flux in supersonic flows for different thermal boundary conditions, AIAA SciTech Forum **2023**, 0868 (2023).

[55] N. Manzano-Miura, D. Gloutak, and G. P. Bewley, Characterization of a turbulent flow with independent variation of Reynolds and Mach numbers, Exp. Fluids **63**, 44 (2022).

[56] J. Christensen-Dalsgaard Jr., W. Dappen, S. V. Ajukov, E. R. Anderson, H. M. Antia, S. Basu, V. A. Baturin, G. Berthomieu, B. Chaboyer, S. M. Chitre, A. N. Cox, P. Demarque, J. Donatowicz, W. A. Dziembowski, M. Gabriel, D. O. Gough, D. B. Guenther, J. A. Guzik, J. W. Harvey, F. Hill, G. Houdek, C. A. Iglesias, A. G. Kosovichev, J. W. Leibacher, P. Morel, C. R. Proffitt, J. Provost, J. Reiter, E. J. Rhodes, Jr., F. J. Rogers, W. Roxburgh, M. J. Thompson, and R. K. Ulrich, The current state of solar modeling, Science **272**, 1286 (1996).

Correction: The first part of Eq. (8) contained an error and has been fixed. A definition of the notation introduced here was also provided.